Operational Limits of Redox Metal Oxides Performing Thermochemical Water Splitting

Alicia Bayon[a,*], *Alberto de la Calle*[b], *Ellen B. Stechel*[c] *and Christopher Muhich*[a*]

Corresponding Authors: Dr. Alicia Bayon, Dr. Christopher Muhich
Muhich Lab, Chemical Engineering, School for the Engineering of Matter Transport and Energy, Arizona State University, ERC 257, 551 E. Tyler Mall, Tempe, AZ, 85281, USA
E-mail: abayonsa@asu.edu ; cmuhich@asu.edu

Dr. Alberto de la Calle
ASU LightWorks®, Arizona State University, PO Box 875402, Tempe, AZ 85281-5402, United States

Dr. Ellen B. Stechel
ASU LightWorks® and the School of Molecular Sciences, Arizona State University, PO Box 875402, Tempe, AZ 85287-5402, USA

Keywords: solar energy, thermochemical cycles, hydrogen production, thermodynamic properties, water splitting

Solar thermochemical hydrogen production is an attractive technology that enables the storage of intermittent solar energy in the form of chemical bonds. Efficient operation requires the identification of a redox-active metal oxide (MO_x) material that can achieve high conversion of water to hydrogen at minimal energy input. Water splitting occurs by consecutive reduction and re-oxidation reactions of a MO_x. The MO_x is reduced to $MO_{x-\delta}$ and, in the second step, is re-oxidized by water to recover the initial MO_x and generate H_2. The material must reduce to $MO_{x-\delta}$ at temperatures achievable in concentrated solar receiver/reactors, while maintaining a thermodynamic driving force to split water. At equilibrium, extent of reduction depends on temperature and oxygen partial pressure, and in this analysis, a set of thermodynamic properties, namely enthalpy, and entropy of oxygen vacancy formation, is sufficient to represent the MO_x. The work presented here is a method to easily classify materials based on these thermodynamic properties under any condition of oxygen partial pressure and temperature. This method is based on fundamental thermodynamic principles and it is applicable for any redox material with known thermodynamic properties. Despite the simplicity of the method,

we believe this analysis will support future research in targeting thermodynamic properties of redox active metal oxides.

1. Introduction

Solar energy is the most abundant and inexhaustible resource on Earth. The solar irradiation reaching the Earth´s surface is about 180 PW, which is between 7000 and 8000 times larger than the current rate of energy consumption [1]. However, the intermittent nature of solar energy poses a challenge as the energy produced must match the energy demand. One way to store solar energy is to split water and convert it into "green" hydrogen. Advanced water splitting (WS) technologies are mostly comprised of photochemical, electrochemical, thermochemical, or a combination of these.[2] Photochemical approaches use solar photons while electrochemical approaches first require the transformation of primary energy into electricity. [3],[4] Thermochemical processes generally use concentrated solar thermal energy to drive the reactions. Thermolysis of water is the direct splitting into hydrogen and oxygen in a single thermally-driven step, which requires very high temperatures (2573 K) to achieve a significant degree of conversion (~5%), and requires a challenging *in-situ* separation of hydrogen and oxygen. [5] Thermochemical cycles divide the thermally-driven WS into a series of consecutive chemical reactions (steps) that release oxygen and hydrogen separately, either temporally or spatially. In this series of reactions, water is consumed while one or more materials actively participate in the process and are regenerated in every cycle.[6] The most simple configuration of a thermochemical cycle uses a metal oxide that reduces and re-oxidizes in two consecutive steps [7]:

$$MO_x \rightarrow MO_{x-\delta} + \frac{\delta}{2} O_2 \quad (1)$$

$$MO_{x-\delta} + \delta H_2O \rightarrow MO_x + \delta H_2 \quad (2)$$

The first reaction (Equation 1) is endothermic and can use concentrated solar energy to provide the heat required to reduce the material ($MO_{x-\delta}$) and generate oxygen. The re-oxidation reaction is

performed by adding water (Equation 2), producing hydrogen, and regenerating the original material (MO_x). The endothermic reaction occurs at significantly lower temperature than water thermolysis (e.g., from 2573 K down to 1773 K) mitigating the challenges associated with extremely high temperatures in addition to avoiding the recombination reaction of H_2 and O_2.[8] Thermochemical cycles can be driven by two or more consecutive reactions. With more than two steps, the endothermic reaction temperature decreases significantly,[9]–[11] but increases the energy losses associated with each step and decreases the solar-to-fuel efficiency.[12] For this reason, two-step redox-active metal oxide thermochemical cycles are currently the most attractive processes for thermochemical WS.

The metal oxides performing two-step thermochemical reactions must have a sufficiently endothermic energy to split water effectively. [13] From the redox-active metal oxide candidates, only a few are applicable in practice. Thermochemical cycles based on metal oxide systems such as ZnO/Zn, SnO_2/SnO, and CdO/Cd, involve reduced metals or metal oxides having a low vapor pressure (Zn; SnO and Cd), producing gaseous compounds that are difficult to recover or separate from the evolved oxygen.[14] The Fe_2O_3/FeO thermochemical cycle undergoes water splitting reactions at reasonable temperatures and oxygen partial pressures;[15] however, it suffers from severe sintering after several thermal cycles and reactivity with water is limited to the near surface region.[16] Adding dopants to iron oxide can reduce sintering, temporarily.[17] $NiFe_2O_4$, $CoFe_2O_4$ and other ferrites have been intensively studied in the literature, [18]–[21] but still show signs of sintering after dozens of cycles. [22]

The first thermochemical cycle demonstrating an extended long term performance under solar radiation was the $CeO_2/CeO_{2-\delta}$ [23]. Unlike previous materials, CeO_2 reduces by producing oxygen vacancies in its lattice. Among other properties, CeO_2 demonstrated reproducible hydrogen production, fast kinetics, and long-term sintering resistance.[23] CeO_2 has also been substituted or doped to increase the oxygen non-stoichiometry and hydrogen productivity [24]–[28].

Recently, perovskite metal oxides (ABO_3) have demonstrated the ability to split water with reduction temperatures lower than CeO_2 [7],[29]–[31]. The thermodynamic properties of perovskites are tunable by altering their chemical composition, with substitutions or dopants on either or both the A and B sites, altering the thermodynamics and therefore permitting different optimal operating conditions [7]. Within the perovskites used for water splitting, formulations using La and Mn on the A site and B sites, respectively, have been extensively investigated.. [32]–[35] First, pioneering work demonstrated that $La_xSr_{1-x}Mn_yAl_{1-y}O_3$ was able to split water at the relatively reduction low temperature of 1350 ^oC [35] producing a larger amount of hydrogen per gram of metal oxide than ceria reduced at a higher temperature. [36] Additional work has demonstrated water splitting of perovskites based on Ba, Ce, Ca and Y on the A site and these species in combination with La [37]–[39]. However, most of these articles did not measure or estimate the water conversion of each cycle; therefore the comparison with ceria or other materials is insufficient to conclude superior performance of a material because water conversion directly effects several large energy costs to the system, such as steam heating and H_2/H_2O separation.

Comparing materials effectively is an arduous task because it requires *a priori* knowledge about the optimal operating partial pressures and temperatures for both reduction and water splitting reactions and their ability to split water with a certain conversion. Several thermodynamic analyses have been performed to elucidate the operational conditions that maximize the solar-to-hydrogen (or fuel) conversion efficiency.[40]–[46] These thermodynamic analyses have been performed mostly for CeO_2. Bader et al. [47] pioneered a steady-state thermodynamic analysis for hydrogen production using concentrated solar thermal, which was followed by many other works using a similar methodology.[40],[41],[48]–[50] Recently, these system models have been expanded to include the co-production of hydrogen and electricity. [51],[52] Dynamic system models of a full concentrated solar thermal plant based on ceria have also been reported, [42],[43],[53],[54] and a few works have covered more than one material in their analysis, [46] thus enabling comparisons of material performance.

However, these thermodynamic analyses require considerable time and resources to explore every single material. Furthermore, they require detailed thermodynamic descriptions of the materials.

A route for rapid evaluation of materials that could allow screening thousands of metal oxides in a wide range of operational temperatures and oxygen partial pressures. Meredig and Wolverton performed pioneering work in materials thermodynamics [55] that was later extended by other authors [56],[57]. These works found temperature and oxygen partial pressure regimes for which the thermal reduction and gas-splitting steps of thermochemical cycles are thermodynamically favorable in terms of the enthalpy and entropy of metal oxide reduction, which represents a valuable materials design goal. They also found that several driving forces, including low thermal reduction oxygen partial pressure and a large positive solid-state entropy of reduction of the metal oxide, have the potential to enable future, more promising two-step gas-splitting cycles. This manuscript aims to extend their framework to include the effects of variable oxygen vacancy formation enthalpy and entropy (Δh_o and Δs_o) allowing a general description for non-stoichiometric materials in a wide range of conditions under counter current operation. Additionally, this work will extend the exploration of the properties studied in [55]–[57], without any selection of the initial operational conditions. We elucidate the effects of the oxygen partial pressure and temperature on the thermodynamic properties (Δh_o and Δs_o). At the end of the article, we compare the state-of-the-art materials in terms of operational conditions, motivating the exploration of materials with targeted thermodynamic properties.

2. Methodology

This work extends the thermodynamic analysis performed by Bayon et al. [7] which is based on fundamental thermodynamic principles and it is applicable for any redox material. Chemical equilibrium of a reaction is defined by a difference in Gibbs free energy of 0:

$$\Delta g = \sum_i \mu_i \Delta x_i = 0 \qquad (3)$$

where μ_i is the chemical potential of the species i and x_i the molar fraction of the substances in equilibrium. The chemical potential is defined as:

$$\mu_i = \begin{cases} g^\circ{}_i + RT \ln a_i \ (if\ solid) \\ g^\circ{}_i + RT \ln(p_i/p^\circ) \ (if\ gas) \end{cases} \quad (4)$$

where $g^\circ{}_i$ is the standard Gibbs free energy of formation of this species, a_i is the activity, p_i is the partial pressure of this species and p° is the reference pressure. The chemical equilibrium of the thermal reduction reaction per mol of oxygen at T_{red} and $p_{\mathrm{O}_2,red}$ can be expressed by:

$$\Delta g_{o,red} = \Delta g^\circ{}_{MO} + \frac{1}{2} g^\circ{}_{O_2} + \frac{1}{2} RT_{red} \ln\left(\frac{p_{\mathrm{O}_2,\mathrm{red}}}{p^\circ}\right) = 0 \quad (5)$$

where we assume that the activities of the reduced and oxidized form of the MO are unity and $\Delta g^\circ{}_{MO} = g^\circ{}_{MO_{red}} - g^\circ{}_{MO_{ox}}$. Defining the Gibbs free energy of the oxygen vacancy formation at standard pressure as:

$$\Delta g_o = \Delta g^\circ{}_{MO} + \frac{1}{2} g^\circ{}_{O_2} \quad (6)$$

Additionally, Δg_o can be defined in terms of enthalpy (Δh_o) and entropy (Δs_o):

$$\Delta g_o = \Delta h_o - T\Delta s_o \quad (7)$$

Note that Δh_o and Δs_o are defined for a fixed value of δ. Substituting Equation 6 and 7 into 5 gives:

$$\Delta h_{o,red} - \Delta s_{o,red} T_{red} = -\frac{1}{2} RT_{red} \ln\left(\frac{p_{\mathrm{O}_2,\mathrm{red}}}{p^\circ}\right) \quad (8)$$

The chemical equilibrium at the re-oxidation reaction conditions, $T_{ox}, p_{\mathrm{H}_2,ox}$, and $p_{\mathrm{H}_2O,ox}$, is given by the following expression:

$$\Delta g_{o,ox} = -\Delta g^\circ{}_{MO} - g^\circ{}_{H_2O} + g^\circ{}_{H_2} - RT_{ox} \ln\left(\frac{p_{H_2O,ox}}{p^\circ}\right) + RT_{ox} \ln\left(\frac{p_{H_2,ox}}{p^\circ}\right) = 0. \quad (9)$$

The Gibbs free energy of the water splitting at standard pressure is defined by:

$$\Delta g^{\circ}_{WS} = g^{\circ}_{H_2} + \frac{1}{2} g^{\circ}_{O_2} - g^{\circ}_{H_2O} \quad (10)$$

where Δg°_{WS} can also be defined in terms of the equilibrium constant (K_{WS}) as:

$$\Delta g^{\circ}_{WS} = -RT_{ox} \ln K_{WS} \quad (11)$$

Finally, substituting Equation 10 and 11 into 9, we obtain the following expression:

$$\Delta g_{o,ox} = -RT_{ox} \ln K_{WS} - \Delta g_o + RT_{ox} \ln \left(\frac{p_{H_2,ox}}{p_{H_2O,ox}} \right) = 0 \quad (12)$$

The H_2O to H_2 splitting conversion is defined as:

$$\theta = \frac{n_{H_2}}{n_{H_2O,in}} \quad (13)$$

which can be substituted in Equation 12:

$$\Delta g_{o,ox} = -RT_{ox} \ln K_{WS} - \Delta g_o + RT_{ox} \ln \left(\frac{\theta}{1-\theta} \right) = 0 \quad (14)$$

Finally, replacing $-\Delta g_o$ of Equation 7 into 14 and subtracting both equalities:

$$\Delta h_{o,\mathrm{ox}} - \Delta s_{o,\mathrm{ox}} T_{ox} = -RT_{ox} \ln\left(\frac{1-\theta}{\theta} K_{WS}\right) \tag{15}$$

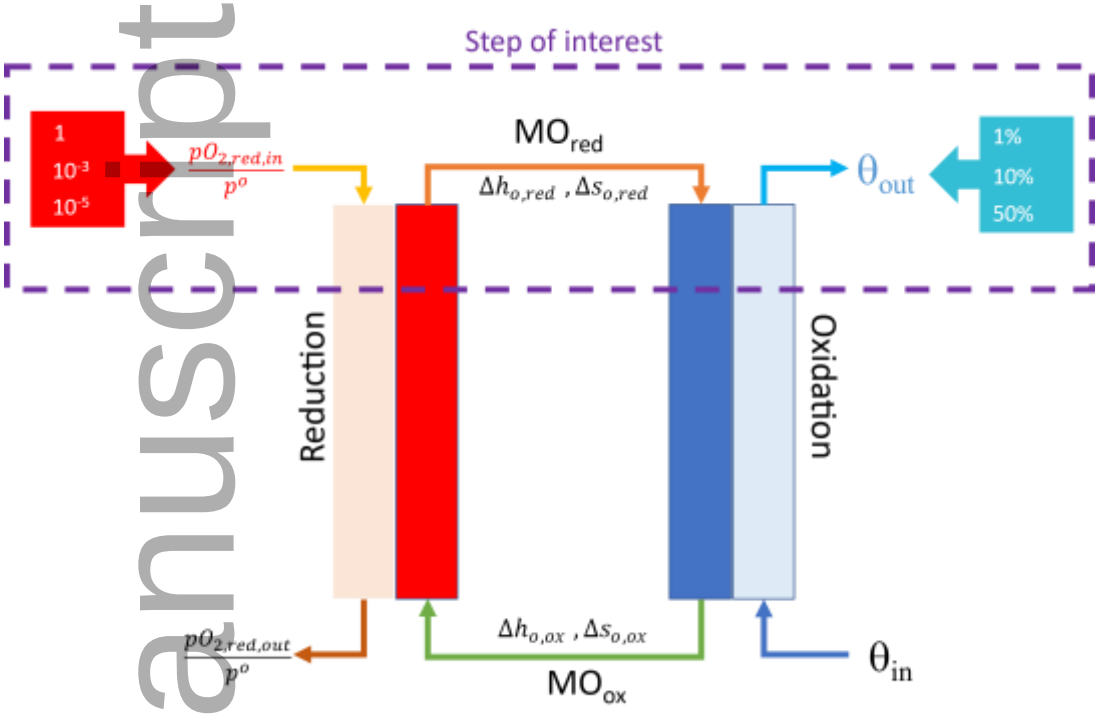

Figure 1: Thermodynamic system of a thermochemical cycle based on redox reactions without knowing the thermodynamic properties a priori. The step of interest is highlighted together with the input variables.

Figure 1 illustrates a thermodynamic system model of the thermochemical water splitting cycle. Even with unknown material properties, we can determine the operational temperatures and partial pressures given a set of assumptions and constraints that reduce the number of degrees of freedom:

1. Conservation of mass and energy in both reactors (physical requirement).
2. Counter current operation (best case scenario) in both reactors, reduction, and re-oxidation.
3. Infinitely fast chemical kinetics.
4. Constant temperature in both reactors: T_{red} and T_{ox}.
5. Inlet partial pressure of oxygen for the reduction reaction and outlet H_2/H_2O conversion ratio are model inputs.

6. Equilibrium conditions are reached at the outlet of the reduction reactor and at the inlet of the re-oxidation reactor. The inlet of the reduction reactor and the outlet of the re-oxidation reactor is out of the scope of this work.
7. Δh_o and Δs_o are functions of the extent of reduction (δ), but independent of temperature.

As explained by Li et al. [58], the second and fourth assumptions can lead to a violation of the local Gibbs criterium when assuming chemical equilibrium at both ends of a counter current reactor. Here, we explicitly avoid that situation by making one of the ends of the reactor flexible; however, this avoidance comes at a cost, namely being unable to calculate the extent of reduction throughout the reactors.

Since the extent of reduction at the outlet of the reduction reactor and the inlet of the re-oxidation reactor is the same, Δh_o and Δs_o must be the same at both points. Therefore, the system is fully determined by the following two equations:

$$\Delta h_o - \Delta s_o T_{red} = -\frac{1}{2} R T_{red} \ln\left(\frac{p_{\mathrm{O_{2,red,in}}}}{p^\circ}\right) \quad (16)$$

$$\Delta h_o - \Delta s_o\, T_{ox} = -R T_{ox} \ln\left(\frac{1-\theta_{out}}{\theta_{out}} K_{WS}\right) \quad (17)$$

Note that $\frac{p_{O_{2,red,in}}}{p^\circ}$ and θ_{out} are model inputs. Equations 16 and 17 allows for the determination of the reduction and re-oxidation temperatures for a pair of Δh_o and Δs_o. Figure 2a shows the effect of $\frac{p_{O_2}}{p^\circ}$ and T_{red} in the logarithmic factor of Equation 16. For the reduction reaction to reach equilibrium, $\Delta h_o - \Delta s_o T_{red}$ must be equal to this factor. Figure 2b shows the effect of θ and T_{ox} in the logarithmic factor of Equation 17. For the re-oxidation reaction to reach equilibrium, $\Delta h_o - \Delta s_o T_{ox}$ must equal this factor.

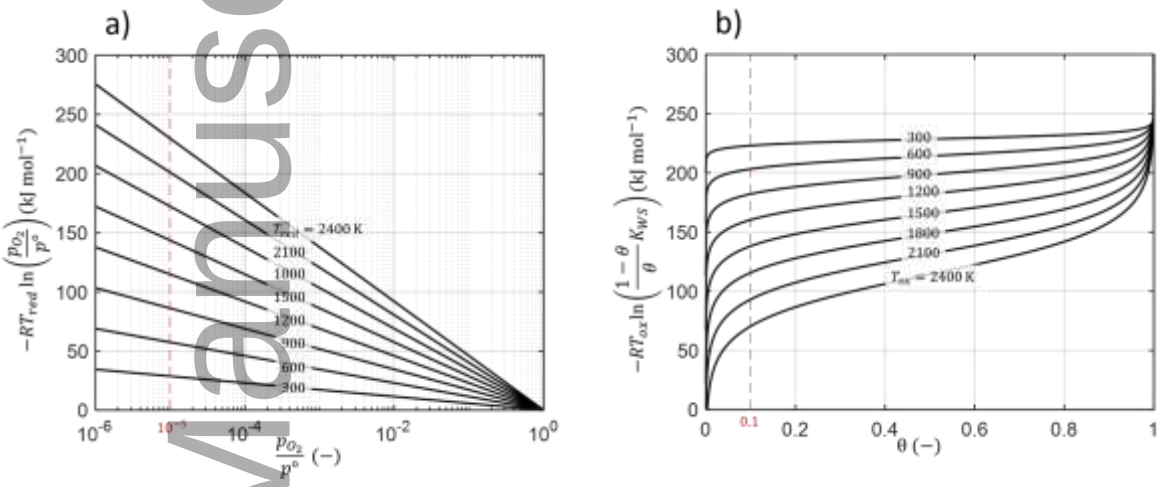

Figure 2: (a) Dependence of the logarithmic factor in Equation 16 on $\frac{p_{O_2}}{p^\circ}$ and T_{red}. (b) Dependence of the logarithmic factor in Equation 17 on θ and T_{ox}.

3. Results

This work aims to identify the properties Δh_o and Δs_o, when the material exits the reduction reactor and enters the re-oxidation reactor, necessary to achieve water splitting. These properties are the most critical in the process and it is reasonable to assume that the rest of the process will occur spontaneously when they are sufficient to split water at the inlet of the re-oxidation reactor. First, we consider the effect of reduction pressure on Δh_o and Δs_o then we will discuss the temperature and partial pressures required to operate water splitting cycles for a given set of Δh_o and Δs_o. Lastly, we consider this methodology in the context of known materials.

3.1. Results at reduction $\frac{p_{O_{2,red,in}}}{p^\circ}$ *= 10^{-5}*

Using Equations 16 and 17, Δh_o can be obtained from Δs_o and temperatures of reduction and re-oxidation separately. To study the effect of these system variables, we hold fixed the reduction oxygen partial pressure at the inlet of the reduction reactor and the conversion of water into hydrogen (θ) leaving the re-oxidation reactor. This section reports the system effects for a reduction oxygen partial pressure of $\frac{p_{O_2,red,in}}{p^o}$ = 10^{-5} and a value of conversion from H_2O to H_2 of θ_{out} = 10%.

Figure 3a and b show the values of the resulting thermodynamic properties. For the thermal reduction (Figure 3a) the thermodynamic properties depend on the value of $\frac{1}{2}RT_{red}\ln\left(\frac{p_{O_2,red,in}}{p^\circ}\right)$, which is represented by the logarithmic curves. As expected, in the thermal reduction reaction, lower Δh_o and higher Δs_o lower the reduction temperature. Conversely, larger Δh_o and lower Δs_o require higher reduction temperatures.

For the re-oxidation, the thermodynamic properties follow a similar trend. The where lower Δh_o and the higher Δs_o require lower re-oxidation temperatures. Conversely, larger Δh_o and lower Δs_o need higher the re-oxidation temperatures. The Δh_o and Δs_o are limited by $RT_{ox}\ln\left(\frac{1-\theta_{out}}{\theta_{out}}K_{WS}\right)$. As shown in Figure 3Figure 3b, for θ_{out}= 10%, a Δh_o of 260 kJ mol^{-1} requires a nearly constant Δs_o = 81 J mol^{-1} K^{-1} is required for operation at temperatures above 800 K. Simultaneously low Δh_o and low Δs_o lowers the re-oxidation temperature.

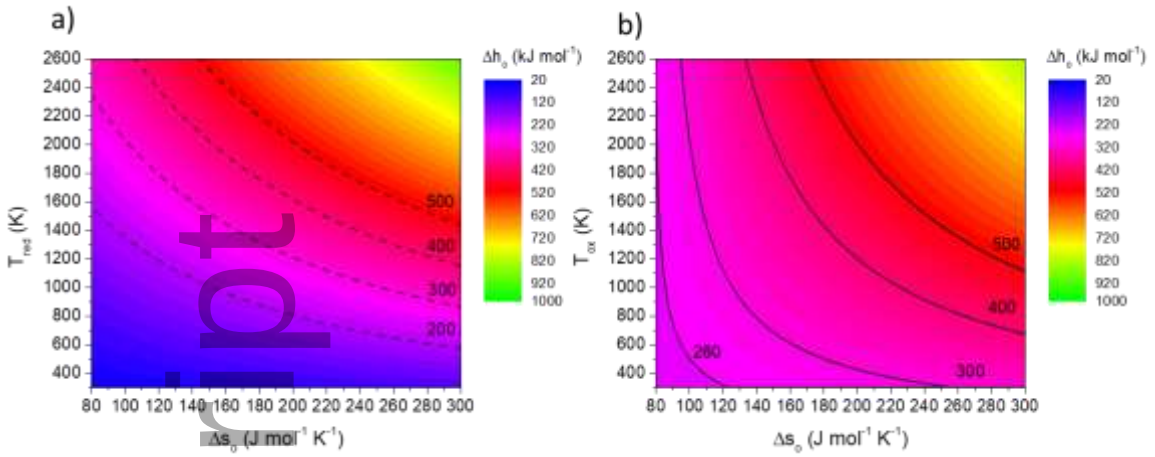

Figure 3: Values Δh_o as a function of Δs_o and the temperatures of (a) reduction and re-oxidation (b). Thermal reduction with fixed $\frac{p_{O_2,red,in}}{p^o}$ = 10^{-5} and the water conversion θ_{out} = 10%. Solid line shows Δh_o are values of 200, 300, 400 and 500 kJ mol^{-1}.

By overlapping the equilibriums shown in Figure 3, we can obtain Figure 4. Generally, higher Δh_o and lower Δs_o results in lower temperature differences between reduction and re-oxidation (note the difference of the height in the dashed and solid lines for 300, 400 and 500 kJ mol^{-1}). Only with high reduction temperatures is it possible to split water at high re-oxidation temperatures. Lowering the reduction temperature results in an increased temperature difference between reduction and re-oxidation (see distance between both dashed and solid lines in Figure 4)

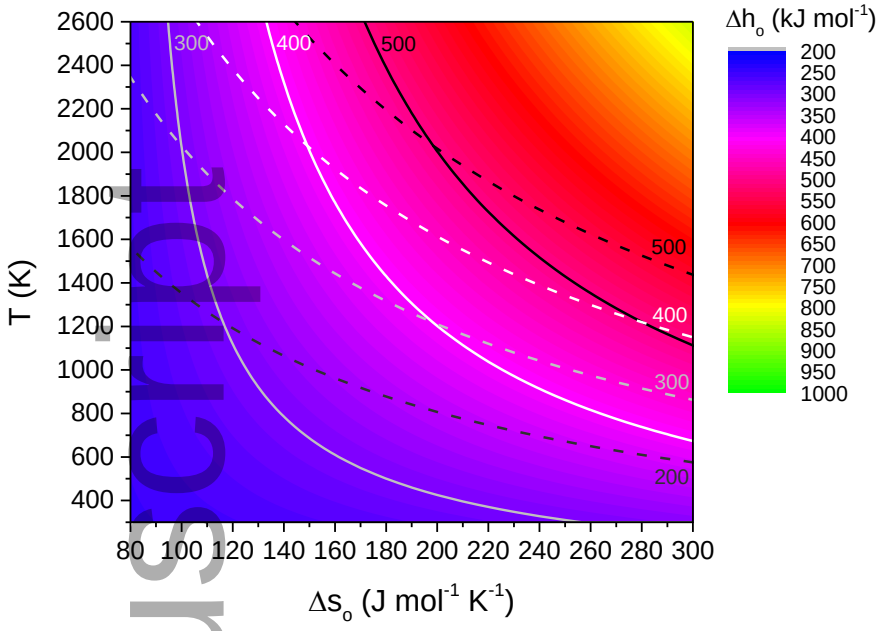

Figure 4: Overlapping of both equilibriums for several values of Δh_o and Δs_o. The thermal reduction is represented by dashed lines of $\frac{p_{O_2,red,in}}{p^o} = 10^{-5}$ and re-oxidation is represented by solid lines (θ_{out} = 10%). Lines highlighted shows Δh_o values of 200, 300, 400 and 500 kJ mol^{-1}.

There is an intersection of both equilibriums at a specific temperature (see intersection between solid and dashed lines for the same values of Δh_o in Figure 4). That is the isothermal operational temperature, which is met when $\frac{1}{2}\ln\left(\frac{p_{O_2,red,in}}{p^o}\right) = \ln\left(\frac{1-\theta_{out}}{\theta_{out}} K_{ws}\right)$. Isothermal water splitting will only be possible, for a conversion of 10% of water, at a temperature of 2030 K and for unique pairs of of Δh_o and Δs_o values. The pairs of Δh_o and Δs_o are: 300 kJ mol^{-1} and 100 J mol^{-1} K^{-1}; 400 kJ mol^{-1} and 149 J mol^{-1} K^{-1}; and 500 kJ mol^{-1} and 200 J mol^{-1} K^{-1}. There are no materials in the literature that can meet the isothermal criteria for a reduction pressure of $\frac{p_{O_2,red,in}}{p^o} = 10^{-5}$ and θ_{out} = 10% during re-oxidation. Either the values of entropy at a given enthalpy are too high or the values of enthalpy at a given entropy are too low. Table 1 shows some examples of pairs of Δh_o and Δs_o values for known materials. Above that intersection of oxygen partial pressures, we could potentially re-oxidize the material at a higher temperature than the reduction.

Table 1: Thermodynamic properties (Δh_o and Δs_o) for materials found in the literature at a specific δ. Displayed are the equilibrium temperatures calculated from Equations 16 and 17 for fixed $\frac{p_{O_{2,red,in}}}{p^o} = 10^{-5}$ in reduction and θ_{out} =10%.

Material	Chemical Formula	Δh_o (kJ mol^{-1})	Δs_o (J mol^{-1} K^{-1})	δ	T_{red} (K)	T_{ox} (K)	ΔT (K)	Ref
Ceria 1	$CeO_{1.9186}$	410	176	0.0814	1833	1590	243	[29]
Ceria 2	$CeO_{1.9427}$	420	191	0.0573	1762	1475	287	[29]
Ceria – Zr5	$(Ce_{0.95}Zr_{0.05})O_{1.9583}$	397	188	0.0417	1683	1304	379	[29]
Ceria – Zr20	$(Ce_{0.80}Zr_{0.20})O_{1.9116}$	357	158	0.0884	1734	1294	440	[29]
Ceria – Nb10	$(Ce_{0.90}Nb_{0.10})O_{1.9852}$	414	212	0.0148	1593	1199	393	[59]
Ceria – Y10	$(Ce_{0.90}Y_{0.10})O_{1.9899}$	444	230	0.0101	1598	1254	344	[59]
Ceria – La10	$(Ce_{0.90}La_{0.10})O_{1.9859}$	453	235	0.0141	1602	1271	330	[59]
LSM10	$(La_{0.90}Sr_{0.10})MnO_{2.9502}$	327	134	0.0498	1798	1311	486	[29]
LSM40	$(La_{0.60}Sr_{0.40})MnO_{2.93}$	270	128	0.07	1603	656	951	[29]
LSM50	$(La_{0.50}Sr_{0.50})MnO_{2.93}$	242	110	0.07	1533	303*	1230	[29]
LSM6464	$(La_{0.6}Sr_{0.4})(Mn_{0.6}Al_{0.4})O_{2.9511}$	282	150	0.0489	1425	1000	425	[29]

**Do not converge for $\Delta g_{o,ox}$ = 0 in the range of T_{ox} from 300 to 3000 K, returns negative value.*

To understand how some materials have successfully demonstrated isothermal water splitting, we next consider 1% water conversion (Figure 5). First, for θ_{out} = 1%, the isothermal splitting temperature decreases considerably to values around 1746 K, which is a common temperature for

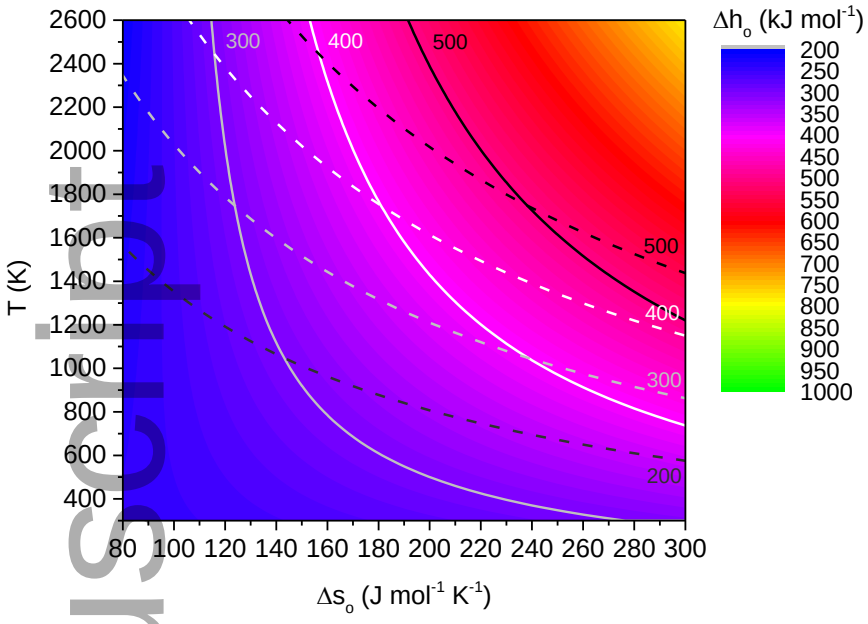

Figure 5: Values of Δh_o and Δs_o to fulfill reduction and water splitting equilibrium. Dashed lines represent thermal reduction for $\frac{p_{O_{2,red,in}}}{p^o}$ = 10^{-5} and solid lines represent water splitting with water conversion θ_{out} = 1%. Highlighted lines are for Δh_o values of 200, 300, 400 and 500 kJ mol^{-1}.

conducting such experiments [60],[61]. The pair of thermodynamic properties are closer to the experimental data in Table 1, demonstrating that isothermal splitting is possible at relatively low temperatures with water conversions of 1% or less. The values of Δh_o and Δs_o are: 300 kJ mol^{-1} and 124 J mol^{-1} K^{-1}; 400 kJ mol^{-1} and 181.2 J mol^{-1} K^{-1}; and 500 kJ mol^{-1} and 238.2 J mol^{-1} K^{-1}. As compared to the values of properties for θ_{out} = 10%, now the Δs_o values are higher by ~25%. From the list of materials collected in Table 1, pure ceria, ceria substituted with 5% zirconia, and LSM10 can perform isothermal water splitting at a temperature close to 1746 K (see Table 1). However, isothermal water splitting is not possible if higher water conversions are desirable and therefore, novel materials showing very large Δh_o and very low Δs_o at the same time should be targeted (conditions for isothermal splitting for conversions of 10% were shown above).

Ideally, researchers would target materials that maximize the conversion of water into hydrogen. Therefore, we next consider θ_{out} = 50% (Figure 6). In this case, the water splitting equilibrium lines shift towards lower values of Δs_o. Additionally, the thermodynamic properties consistent with water

splitting are even more restrictive, requiring higher Δh_o and lower Δs_o values as compared to the values at lower conversions, as well as a higher temperature difference between both reactions.

The specific pair of Δh_o and Δs_o when both reactions cross at the isothermal temperature are: 400 kJ mol^{-1} and 120.1 J mol^{-1} K^{-1}; and 500 kJ mol^{-1} and 161.9 J mol^{-1} K^{-1}. In this case, materials with Δh_o equal to 200 kJ mol^{-1} and 300 kJ mol^{-1} will require very low Δs_o. If we compare the values of Δh_o and Δs_o with the materials shown in Table 1, we cannot find any that can meet the isothermal operation with 50% water conversion. The minimum Δs_o for any material having a Δh_o higher than 400 kJ mol^{-1} is 45% larger than 120 J mol^{-1} K^{-1}. However, some materials could work under non-isothermal conditions. Among the materials in the range of 400 to 500 kJ mol^{-1} (see Table 1), the lowest temperature difference will be for pure ceria with a formula $CeO_{1.9186}$.

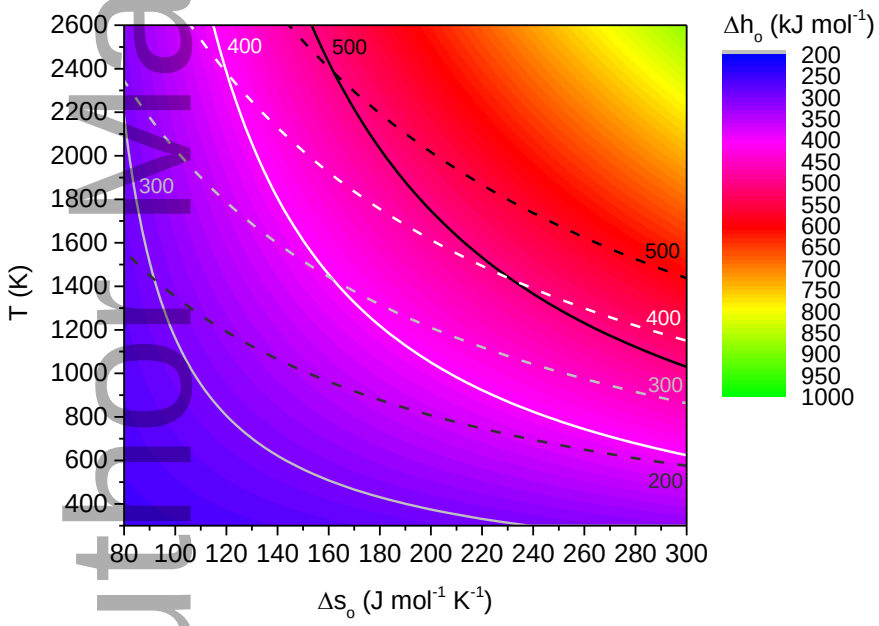

Figure 6: Values of Δh_o and Δs_o to fulfill reduction and water splitting equilibrium. The thermal reduction is represented by dashed lines of $\frac{p_{O_{2,red,in}}}{p^o} = 10^{-5}$ and water splitting is represented by solid lines with a water conversion of θ_{out} = 50%. Lines highlighted shows Δh_o values of 200, 300, 400 and 500 kJ mol^{-1}.

3.2. Results at reduction $\frac{p_{O_{2,red,in}}}{p^\circ} = 10^{-3}$ and 1

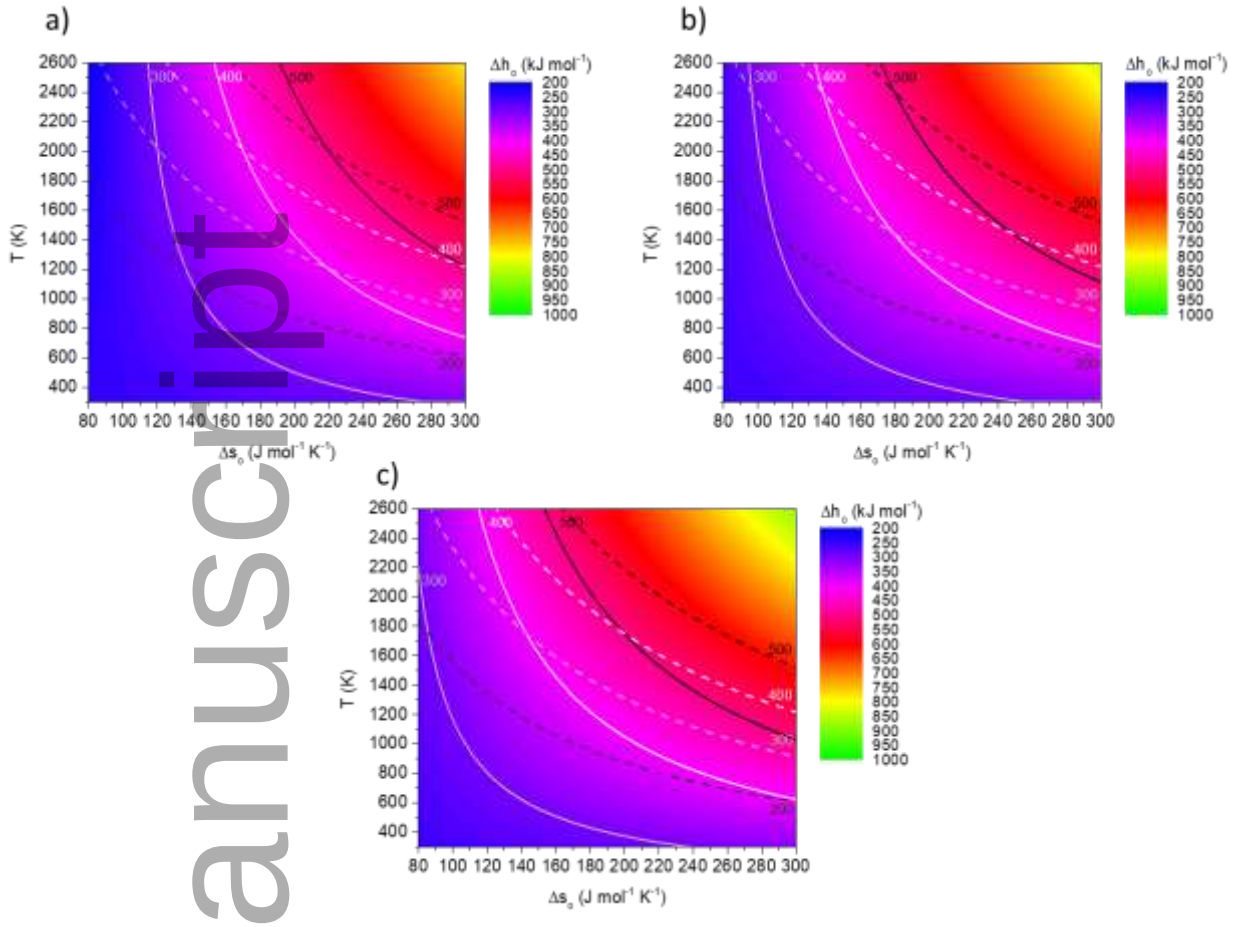

Figure 7: Values of Δh_o and Δs_o to fulfill reduction and water splitting equilibrium (as in Figure 2) with $\frac{p_{O_{2,red,in}}}{p^o}$ = 10^{-3} and θ_{out} = a) 1%, b) 10%, and c) 50%.

Similarly, to the previous section it is possible to calculate analogous curves for milder reduction conditions, e.g., $\frac{p_{O_{2,red,in}}}{p^o}$ = 10^{-3} (see Figure 7). Overall, there is a general shift of the reduction Δh_o to higher T_{red} while maintaining the same logarithmic shape. The temperature difference between both reactions increases as compared to the case of $\frac{p_{O_{2,red,in}}}{p^o}$ = 10^{-5}. This observation means the same materials will require a higher reduction temperature given a higher oxygen partial pressure of reduction to obtain the same degree of non-stoichiometry (δ), which is expected and in agreement to the experimental demonstration [39]. The same conclusion can be obtained for a fixed $\frac{p_{O_{2,red,in}}}{p^o}$ = 1 (Figure 8). The differences between the temperatures of reduction and re-oxidation can be observed at the intersections of the dashed and solid lines in Figure 8 and Figure 9. The separation between the dashed (reduction) and solid (water splitting) equilibrium lines are higher as compared to the example

of $\frac{p_{O_{2,red,in}}}{p^o}$ = 10^{-5}. The isothermal operational temperatures are now: 2008 K and 2600 K for $\frac{p_{O_{2,red,in}}}{p^o}$ = 10^{-3} and 1, respectively, for fixed θ_{out} = 1%. Higher isothermal operational temperatures are required instead of the 1746 K for $\frac{p_{O_{2,red,in}}}{p^o}$ = 10^{-5} and θ_{out} = 1% conversion shown previously. This trend is the same for any reduction temperature in temperature swing operation. For other values of θ_{out}, the required operational temperatures are even higher than for the example of 1% as Figure 6 and Figure 7 show.

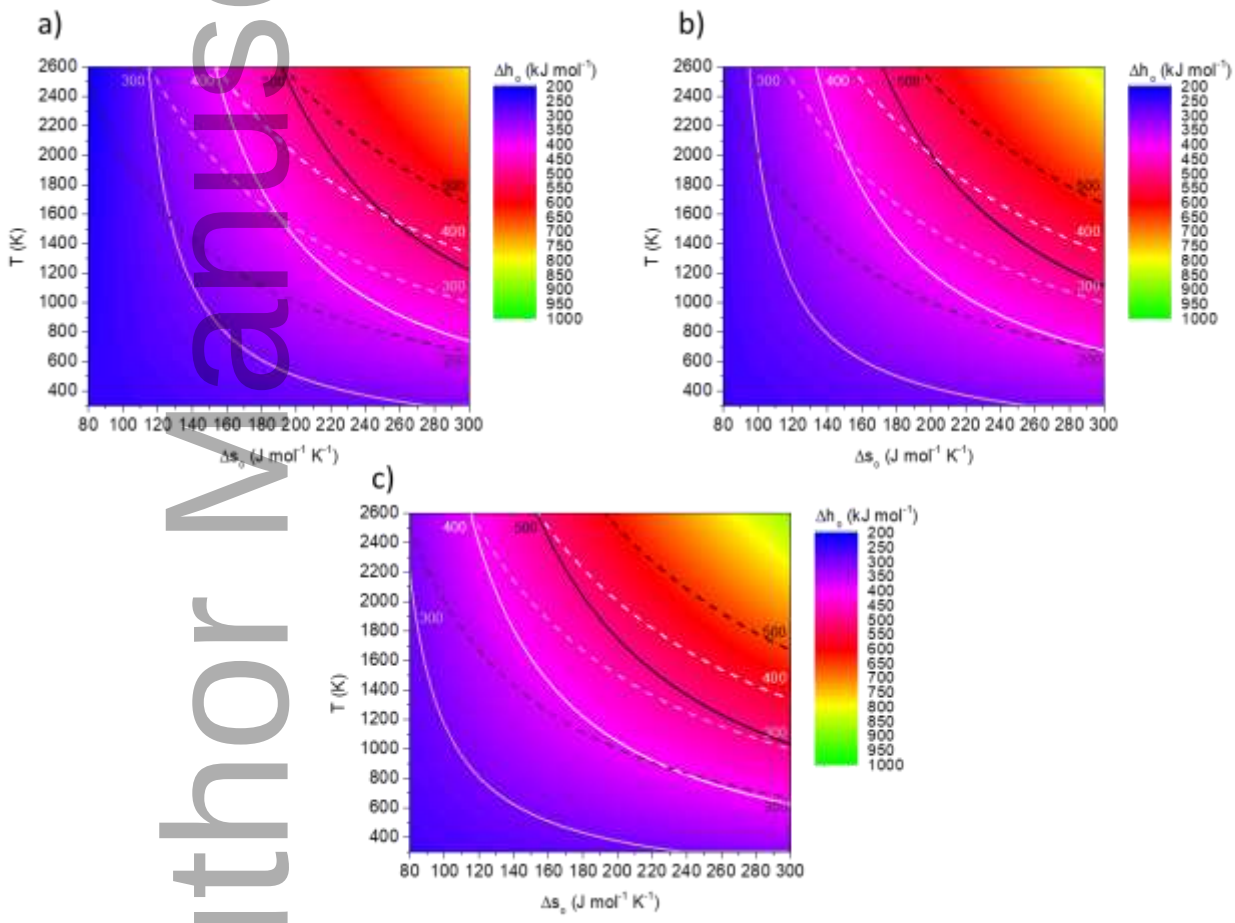

Figure 8: Values of Δh_o and Δs_o to fulfill reduction and water splitting equilibrium (as in Figure 2) with $\frac{p_{O_{2,red,in}}}{p^o}$ = 1 and θ_{out} = a) 1%, b) 10%, and c) 50%.

3.3. Temperatures of equilibrium for reduction and re-oxidation

Following the same methodology, the equilibrium temperatures for each pair of values of Δh_o and Δs_o can be obtained. Figure 9 shows the resulting temperatures for $\frac{p_{O_{2,red,in}}}{p^o}$ of 10^{-5} and θ_{out} = 10%.

First, we observe that the relationship of Δh_o and Δs_o is a straight line with different slopes depending on the value of the $RT\ln\left(\frac{p_{O_2}}{p^o}\right)$. The value of $RT_{red}\frac{1}{2}\ln\left(\frac{p_{O_{2,red,in}}}{p^o}\right)$ varies only with T_{red} as $\frac{1}{2}\ln\left(\frac{p_{O_{2,red,in}}}{p^o}\right)$ is constant in the reduction reaction and the slope does not vary significantly in Figure 9a. However, for the re-oxidation, the slope changes with the value of $RT_{ox}\ln\left(\frac{1-\theta,out}{\theta,out}K_{ws}\right)$ in Figure 9b. The re-oxidation reaction converges to a single value of Δh_o and $T\Delta s_o$ when both are equal to $\ln\left(\frac{1-\theta,out}{\theta,out}K_{ws}\right)$ at any temperature. These values for the example in Figure 9 are close to 260 kJ mol^{-1} and 81 J mol^{-1} K^{-1}.

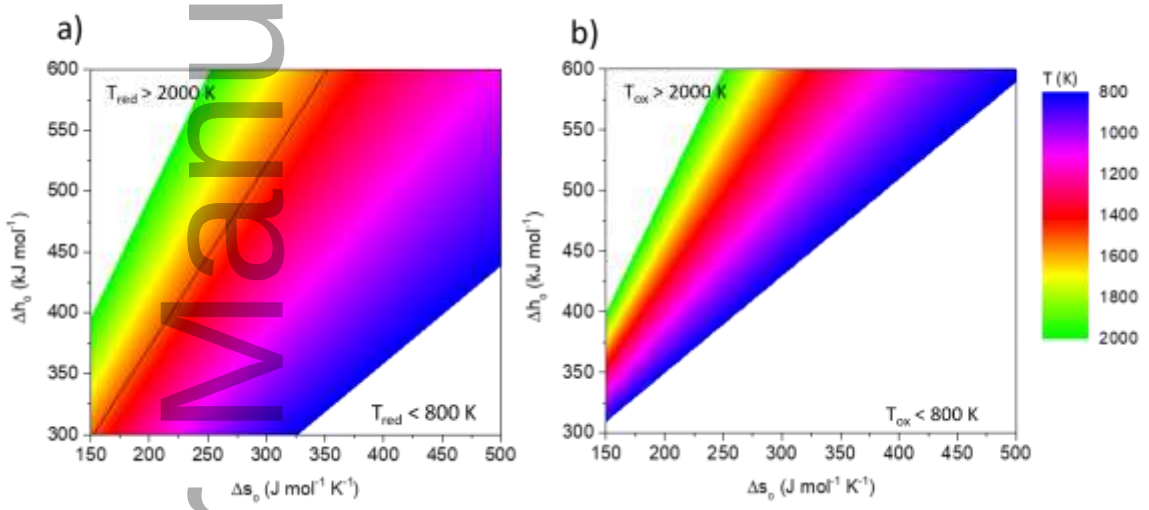

Figure 9: Temperatures of operation for each pair of Δh_o and Δs_o to set $\Delta g_o = 0$ for reduction and water splitting equilibrium: a) reduction temperatures for $\frac{p_{O_{2,red,in}}}{p^o} = 10^{-5}$ and b) re-oxidation temperatures for θ_{out} = 10%. The white background represents temperatures above and below the limits indicated in the graphs. The solid line in a) is 1500 K as a guide for the reader.

For the reduction equilibrium, higher Δh_o directly implies a higher reduction temperature for a constant Δs_o and a higher Δs_o implies a lower reduction temperature for a constant Δh_o. This trend is also true for the re-oxidation equilibrium, but it becomes more evident as Δh_o decreases. For example, for materials with Δh_o = 400 kJ mol^{-1}, lower T_{ox} is achievable only with higher

Δs_o because $\Delta h_o - T_{ox}\Delta s_o = 0$ (see narrower range of Δs_o for a constant value of Δh_o at 400 kJ mol^{-1} as compared to 600 kJ mol^{-1}). This result implies the operational range of temperatures is smaller as well.

Figure 10 shows the overlapping of Figure 9a and b for two different water splitting conversions, 10% and 50% The conversion of 1% is not shown here as it has limited application from a practical point of view.

It can be observed that higher ΔT between reduction and re-oxidation enables a wider region of thermodynamic properties that fulfill both equilibrium requirements. Generally, the higher the water splitting temperature is, the higher the reduction temperature must be (as concluded in the previous section). As the slope of the water equilibrium lines becomes parallel to the reduction equilibrium at very high temperatures (e.g., 1600 K), having materials with adequate properties in the region of extremely high reduction and re-oxidation temperatures becomes very restrictive (see for water splitting/re-oxidation temperature of 1800 K, that the minimum value of Δh_o is 380 kJ mol^{-1} and matches in the reduction temperature of 2000 K in Figure 10a). The same can be observed for higher water conversion (Figure 10Figure 10b) with even more restrictive temperature of operation between reduction and re-oxidation.

It is also possible to observe the minimum reduction temperatures for a given re-oxidation temperature. For a conversion of 10%, and a reoxidation temperature of 1000 K (see dashed line at 1000 K in Figure 10a), the minimum reduction temperature will be 1300 K (see intersection of dashed line of 1000 K with contour temperature of 1300 K at the end of the right-hand side of the Figure 10a). A temperature difference of 300 K together with 1300 K reduction temperature would require values of Δh_o > 530 kJ mol^{-1} and Δs_o > 375 J mol^{-1} K^{-1}. Any other material with lower Δh_o and Δs_o will have a higher reduction temperature (see intersections of 1000 K dashed line with colored line). For materials with a Δh_o of about 400 kJ mol^{-1} (like pure ceria) a minimum reduction temperature will be 1500 K, at the maximum limit of Δs_o, making the minimum ΔT of 500 K (see Figure 10a by

assuming a straight line from 400 kJ mol^{-1} until the dashed line of 1000 K). For values of higher water conversion, a ΔT of 600 K is needed in the same example.

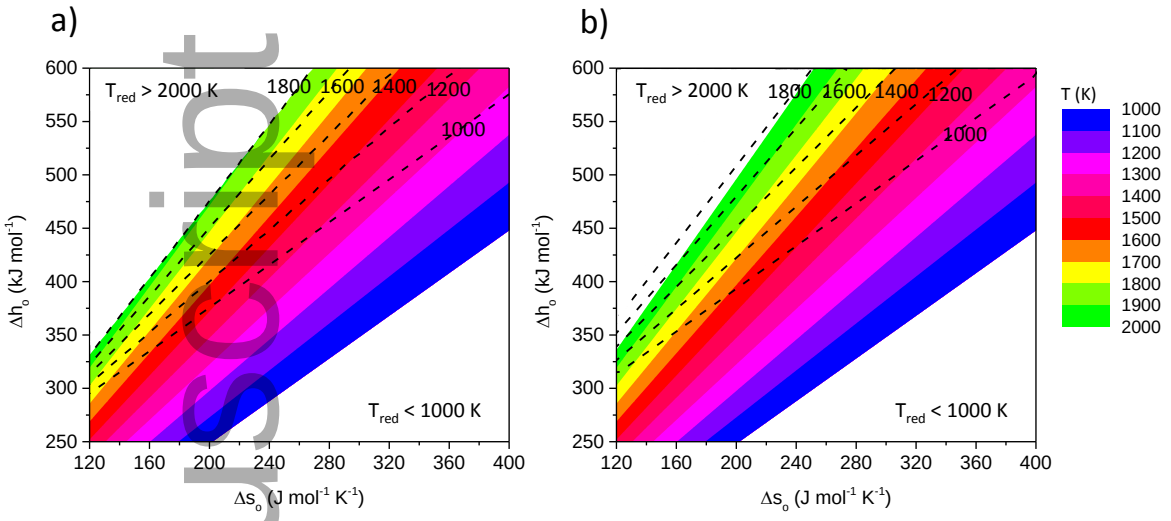

Figure 10: Temperatures of operation for each pair of Δh_o and Δs_o for reduction and water splitting equilibrium with reduction temperatures for a fixed $\frac{p_{O_{2,red,in}}}{p^o}$ = 10^{-5} and re-oxidation/water splitting temperatures for: a) θ_{out} = 10% and b) θ_{out} = 50%.

3.5. Application of fundamental thermodynamic principles to classify known materials

The method applied above can be plotted together with known materials properties for temperatures of operation allowing a quick comparison between them. In Figure 11a and b, $\frac{p_{O_{2,red,in}}}{p^o}$ of reduction is 10^{-5} and θ_{out} = 10%. Figure 11a shows an imposed maximum thermal reduction temperatures of 2000 K and minimum water splitting or re-oxidation reactions temperature of 1000 K . The properties of known materials are shown in dots as per Table 1.

For these wide allowable operating conditions (here the ΔT is set to 1000 K), most of experimentally proven materials (except for LSM40 and LSMA6464) fall in the region of favorable thermodynamic properties. The two perovskites below that require water splitting temperatures below 1000 K. However, if we limit the operational temperatures to 1800 K for reduction and 1400 K for water splitting, representing low temperature swing operation, we observe that only $CeO_{1.9427}$ (named Ceria

2 in Table 1 and Figure 11b) is operable. The closer the temperatures of operation, the harder it is to find appropriate thermodynamic properties and materials.

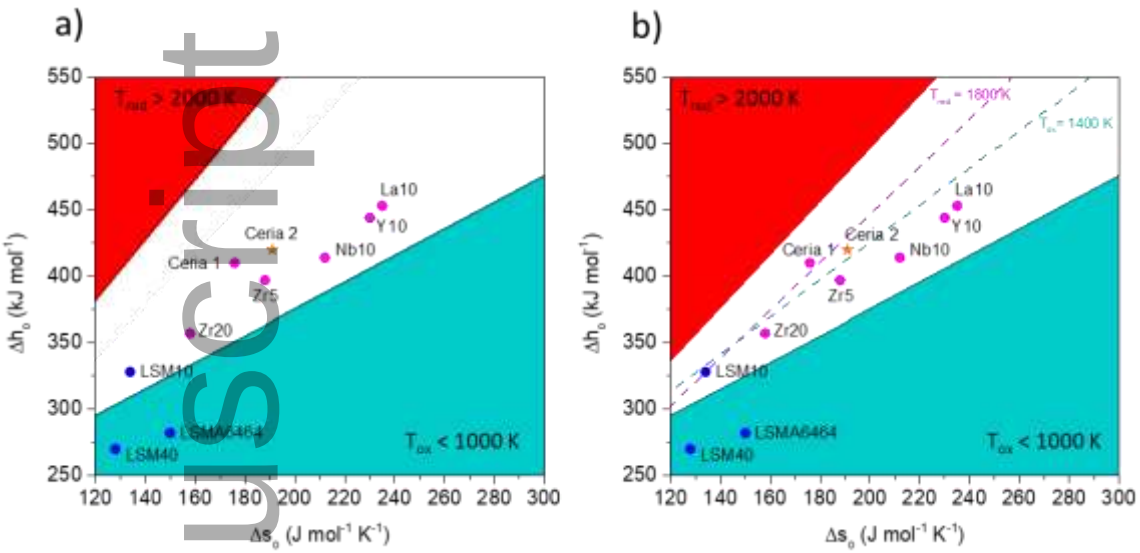

Figure 11: Temperature ranges for each pair of Δh_o and Δs_o to achieve $\Delta g_o = 0$ for reduction and water splitting equilibrium with for fixed $\frac{p_{O_{2,red,in}}}{p^o} = 10^{-5}$ and re-oxidation temperatures for $\theta_{out} = 10\%$. The white background is the region of operation for reduction below 2000 K and re-oxidation above 1000 K (in b) the region between 1800 and 1400 K is highlighted). Dots represent values of selected materials collected in Table 1.

Depending on the targeted operational conditions, this method allows one to obtain different thermodynamic properties plots that will allow them to quickly determine the temperatures of operation given the oxygen partial pressure of reduction and the water conversion. Thus, enabling quick classification of materials, and comparison between them under the same equilibrium assumptions without a complicated description of the system.

4. Conclusions

In this work, we developed a method to easily classify thermodynamic properties for redox-active metal oxide materials capable of two step thermochemical water splitting cycles. This method is based on fundamental thermodynamic principles and it is applicable for any redox material with known thermodynamic properties. An initial investigation is given by the assumption that a set of thermodynamic properties (Δh_o and Δs_o) define the equilibrium of reduction and re-oxidation, with

a fixed oxygen partial pressure at the inlet of the reduction as well as a fixed water conversion at the outlet of re-oxidation.

First, we evaluated the values of Δh_o given T and Δs_o for both reactions in a wide set of conditions. We found that for thermal reduction, higher Δh_o implies a higher reduction temperature for a fixed Δs_o. In contrast, for the same value of Δh_o, higher Δs_o implies a lower temperature of reduction. For the water splitting reaction, we observed that higher Δh_o results in higher temperatures for re-oxidation given a fixed Δs_o. In contrast, for the same value of Δh_o, the higher is Δs_o the lower is the temperature of re-oxidation. The temperature difference between both reactions can be reduced by decreasing Δs_o until isothermal splitting is met for unique pair of values of Δh_o and Δs_o.

This work demonstrates that isothermal splitting is thermodynamically possible, however, it requires materials with Δh_o and Δs_o properties out of the range of experimental values found in the literature for high water conversions. For water conversion of more than 1%, the isothermal splitting temperature will be higher than 1746 K and if the water conversion higher than 10%, then the isothermal temperature is higher than 2030 K. Novel materials with targeted properties are required if isothermal splitting is aimed. For current materials under investigation, isothermal splitting is possible only at low water conversions.

The range of operational thermodynamic properties is wider if a temperature swing operation is considered. If a temperature swing operation is desired, there are 3 different scenarios for targeted properties:

1) If the temperature difference between both reactions is not critical, a low Δh_o and a high Δs_o should be targeted. This set of materials will have a relatively low reduction temperature (e.g., below 1800 K) but at the cost of a low re-oxidation temperature and a large temperature difference. The higher Δs_o is the lower will be the re-oxidation temperature and larger will be the temperature difference. These materials may be like current perovskites found in the literature.

2) If the temperature difference is critical and it is to be minimized, then finding materials with high Δh_o and relatively low Δs_o should be targeted. This result implies that these materials will be reduced at higher temperatures (e.g., above 1800 K) but also oxidized at higher re-oxidation temperatures, reducing the overall temperature difference between both reactions. The lower Δs_o is, the higher the water splitting temperature needs to be, and a smaller temperature difference between the reactions is required. These materials may be like ceria and doped ceria.

3) A low reduction temperature, and, at the same time, a low temperature difference between reactions is thermodynamically favorable only for very large Δh_o and Δs_o. Therefore, if both a low temperature difference and low reduction temperature is desired completely novel materials must be discovered. Note that low reduction temperatures are not always associated with low Δh_o because it depends on Δs_o.

Finally, we conclude that depending on the targeting temperatures, pressures, water conversion and temperature difference between reduction and water splitting, different set of values of Δh_o and Δs_o should be targeted for material design. The method presented here can facilitate the search for these specific properties depending on the operational conditions pursued by the materials under investigation with any *a priori* set of conditions.

Acknowledgements

A.B. and C.M. gratefully acknowledge partial financial support for this work by ARPA-E via the DAYS program through contract No. DE- AR0000991 and by the U.S. Department of Defense. A.B. was partially funded by ASU LightWorks®. E.B.S. and A.C. gratefully acknowledge research and funding support from the HydroGEN Advanced Water Splitting Materials Consortium, established as part of the Energy Materials Network under the U.S. Department of Energy, Office of Energy Efficiency and Renewable Energy, Hydrogen and Fuel Cell Technologies Office, under Award No. DE-EE0008090 and DE–EE0008991, respectively.

References

[1] P. Breeze. *Solar Power*. In *Power Generation Technologies*; Breeze, P., Ed.; Elsevier, 2019; pp 293–321, DOI: 10.1016/B978-0-08-102631-1.00013-4.

[2] Z. Wang, R. R. Roberts, G. F. Naterer, K. S. Gabriel. *Int. J. Hydrogen Energy* **2012**, *37* (21), 16287–16301, DOI: 10.1016/j.ijhydene.2012.03.057.

[3] R. Pinsky, P. Sabharwall, J. Hartvigsen, J. O'Brien. *Prog. Nucl. Energy* **2020**, *123* (February), 103317, DOI: 10.1016/j.pnucene.2020.103317.

[4] X. Xu, W. Wang, W. Zhou, Z. Shao. *Small Methods* **2018**, *2* (7), 1800071, DOI: 10.1002/smtd.201800071.

[5] A. Steinfeld. *Sol. Energy* **2005**, *78* (5), 603–615, DOI: 10.1016/j.solener.2003.12.012.

[6] R. Bhosale, R. Khadka, J. Puszynski, R. Shende. *J. Renew. Sustain. Energy* **2011**, *3* (6), 63104, DOI: 10.1063/1.3659684.

[7] A. Bayon, A. de la Calle, K. K. Ghose, A. J. Page, R. McNaughton. *Int. J. Hydrogen Energy* **2020**, *45*, 12653–12679.

[8] A. de la Calle, A. Bayon. *Int. J. Hydrogen Energy* **2019**, *44* (3), 1409–1424, DOI: 10.1016/J.IJHYDENE.2018.11.076.

[9] A. Bayón, V. A. De La Penã O'Shea, D. P. Serrano, J. M. Coronado. *J. CO2 Util.* **2020**, *42*, DOI: 10.1016/j.jcou.2020.101264.

[10] A. Bayón, V. A. De La Peña O'Shea, J. M. Coronado, D. P. Serrano. *Int. J. Hydrogen Energy* **2016**, DOI: 10.1016/j.ijhydene.2015.09.159.

[11] A. Bayón, V. A. De La Peña O'Shea, D. P. Serrano, J. M. Coronado. *Int. J. Hydrogen Energy* **2013**, DOI: 10.1016/j.ijhydene.2013.07.101.

[12] S. Abanades, P. Charvin, G. Flamant, P. Neveu. *Energy* **2006**, *31*, 2469–2486, DOI: 10.1016/j.energy.2005.11.002.

[13] C. Muhich, A. Steinfeld. *J. Mater. Chem. A* **2017**, *5* (30), 15578–15590, DOI: 10.1039/c7ta04000h.

[14] S. Abanades. *ChemEngineering* **2019**, *3* (3), 63, DOI: 10.3390/chemengineering3030063.

[15] A. Steinfeld, S. Sanders, R. Palumbo. *Sol. Energy* **1999**, *65* (1), 43–53.

[16] E. N. Coker, M. A. Rodriguez, A. Ambrosini, J. E. Miller, E. B. Stechel. *Powder Diffr.* **2012**, *27* (02), 117–125, DOI: 10.1017/S0885715612000255.

[17] J. E. Funk. *Int. J. Hydrogen Energy* **2001**, *26*, 185–190.

[18] S. Lorentzou, G. Karagiannakis, C. Pagkoura, a. Zygogianni, a. G. Konstandopoulos. *Energy Procedia* **2014**, *49*, 1999–2008, DOI: 10.1016/j.egypro.2014.03.212.

[19] N. Gokon, T. Mataga, N. Kondo, T. Kodama. *Int. J. Hydrogen Energy* **2011**, *36* (8), 4757–4767, DOI: 10.1016/j.ijhydene.2011.01.076.

[20] C. L. Muhich, K. C. Weston, D. Arifin, A. H. McDaniel, C. B. Musgrave, A. W. Weimer. *Ind. Eng. Chem. Res.* **2015**, *54* (16), 4113–4122, DOI: 10.1021/ie503894f.

[21] K. M. Allen, N. Auyeung, N. Rahmatian, J. F. Klausner, E. N. Coker. *JOM* **2013**, *65* (12), DOI: 10.1007/s11837-013-0774-1.

[22] N. B. Goikoetxea, M. B. Gómez-Mancebo, R. Fernández-Saavedra, F. Borlaf, F. García-Pérez, J. A. Jiménez, I. Llorente, I. Rucandio, A. J. Quejido. *Int. J. Hydrogen Energy* **2019**, *44* (33), 17578–17585, DOI: 10.1016/j.ijhydene.2019.05.003.

[23] W. C. Chueh, C. Falter, M. Abbott, D. Scipio, P. Furler, S. M. Haile, A. Steinfeld. *Science (80-.).* **2010**, *1797* (December), 1–8, DOI: 10.1126/science.1197834.

[24] R. R. Bhosale, G. Takalkar, P. Sutar, A. Kumar, F. AlMomani, M. Khraisheh. *Int. J. Hydrogen Energy* **2019**, *44* (1), 34–60, DOI: 10.1016/j.ijhydene.2018.04.080.

[25] Y. Hao, C. Yang, S. M. Haile. **2014**, 2–11.

[26] X. Gao, G. Liu, Y. Zhu, P. Kreider, A. Bayon, T. Gengenbach, T. Lu, Y. Liu, J. Hinkley, W. Lipiński, A. Tricoli. *Nano Energy* **2018**, DOI: 10.1016/j.nanoen.2018.05.045.

[27] C. Muhich, M. Hoes, A. Steinfeld. *Acta Mater.* **2018**, *144*, 728–737, DOI: 10.1016/j.actamat.2017.11.022.

[28] D. Arifin, A. Ambrosini, S. A. Wilson, B. Mandal, C. L. Muhich, A. W. Weimer. *Int. J.*

Hydrogen Energy **2020**, *45* (1), 160–174, DOI: 10.1016/j.ijhydene.2019.10.177.

[29] R. J. Carrillo, J. R. Scheffe. *Sol. Energy* **2017**, *156*, 3–20, DOI: 10.1016/j.solener.2017.05.032.

[30] J. R. Scheffe, A. H. McDaniel, M. D. Allendorf, A. W. Weimer. *Energy Environ. Sci.* **2013**, *6* (3), 963, DOI: 10.1039/c3ee23568h.

[31] J. Vieten, B. Bulfin, P. Huck, M. Horton, D. Gubán, L. Zhu, Y. Lu, K. Persson, M. Roeb, C. Sattler. *Energy Environ. Sci.* **2019**, DOI: 10.1039/C9EE00085B.

[32] C.-K. Yang, Y. Yamazaki, A. Aydin, S. M. Haile. *J. Mater. Chem. A* **2014**, *2*, 13612–13623, DOI: 10.1039/c4ta02694b.

[33] J. R. Scheffe, D. Weibel, A. Steinfeld. *Energy & Fuels* **2013**, *27* (8), 4250–4257, DOI: 10.1021/ef301923h.

[34] M. Ezbiri, V. Becattini, M. Hoes, R. Michalsky, A. Steinfeld. *ChemSusChem* **2017**, *10* (7), 1517–1525, DOI: 10.1002/cssc.201601869.

[35] A. H. McDaniel, E. C. Miller, D. Arifin, A. Ambrosini, E. N. Coker, R. O'Hayre, W. C. Chueh, J. Tong. *Energy Environ. Sci.* **2013**, *6* (8), 2424–2428, DOI: 10.1039/c3ee41372a.

[36] J. E. Miller, M. A. Allendorf, A. Ambrosini, E. N. Coker, R. B. Diver, I. Ermanoski, L. R. Evans, R. E. Hogan, A. H. Mcdaniel. *SANDIA Rep. SAN2012-5658* **2012**.

[37] S. Dey, B. S. Naidu, C. N. R. Rao. *Chem. - A Eur. J.* **2015**, *21* (19), 7077–7081, DOI: 10.1002/chem.201500442.

[38] R. D. Barcellos, M. D. Sanders, J. Tong, A. H. McDaniel, R. P. O'Hayre. *Energy Environ. Sci.* **2018**, *11* (11), 3256–3265, DOI: 10.1039/c8ee01989d.

[39] M. Takacs, M. Hoes, M. Caduff, T. Cooper, J. R. Scheffe, A. Steinfeld. *Acta Mater.* **2016**, *103*, 700–710, DOI: 10.1016/j.actamat.2015.10.026.

[40] I. Ermanoski, J. E. Miller, M. D. Allendorf. *Phys. Chem. Chem. Phys.* **2014**, *16* (18), 8418–8427, DOI: 10.1039/c4cp00978a.

[41] I. Ermanoski, N. Siegel. *Energy Procedia* **2014**, *49*, 1932–1939, DOI:

10.1016/j.egypro.2014.03.205.

[42] A. Bayon, A. De La Calle. *AIP Conf. Proc.* **2019**, *2126* (July), DOI: 10.1063/1.5117683.

[43] A. de la Calle, A. Bayon. *Int. J. Hydrogen Energy* **2019**, *44* (3), 1409–1424, DOI: 10.1016/j.ijhydene.2018.11.076.

[44] B. D. Ehrhart, C. L. Muhich, I. Al-Shankiti, A. W. Weimer. *Int. J. Hydrogen Energy* **2016**, *41* (44), 19894–19903, DOI: 10.1016/j.ijhydene.2016.07.110.

[45] B. D. Ehrhart, C. L. Muhich, I. Al-Shankiti, A. W. Weimer. *Int. J. Hydrogen Energy* **2016**, *41* (44), 19894–19903, DOI: 10.1016/j.ijhydene.2016.07.110.

[46] C. L. Muhich, S. Blaser, M. C. Hoes, A. Steinfeld. *Int. J. Hydrogen Energy* **2018**, *43* (41), 18814–18831, DOI: 10.1016/j.ijhydene.2018.08.137.

[47] R. Bader, L. J. Venstrom, J. H. Davidson, W. Lipin, W. Lipiński. *Energy and Fuels* **2013**, *27* (9), 5533–5544, DOI: 10.1021/ef400132d.

[48] P. T. Krenzke, J. H. Davidson. *Energy & Fuels* **2015**, *29* (2), 1045–1054, DOI: 10.1021/ef502601f.

[49] I. Ermanoski, N. P. Siegel, E. B. Stechel. *J. Sol. Energy Eng.* **2013**, *135* (3), 31002, DOI: 10.1115/1.4023356.

[50] B. D. Ehrhart, C. L. Muhich, I. Al-Shankiti, A. W. Weimer. *Int. J. Hydrogen Energy* **2016**, *41* (44), 19904–19914, DOI: 10.1016/j.ijhydene.2016.07.106.

[51] V. K. Budama, N. G. Johnson, I. Ermanoski, E. B. Stechel. *Int. J. Hydrogen Energy* **2021**, *46* (2), 1656–1670, DOI: 10.1016/j.ijhydene.2020.10.060.

[52] V. K. Budama, N. G. Johnson, A. McDaniel, I. Ermanoski, E. B. Stechel. *Int. J. Hydrogen Energy* **2018**, *43* (37), 17574–17587, DOI: 10.1016/j.ijhydene.2018.07.151.

[53] A. de la Calle Alonso, A. Bayon. *Annual Performance of a Solar-Thermochemical Hydrogen Production Plant Based on CeO2 Redox Cycle*; 2017, DOI: 10.3384/ecp17132857.

[54] A. Bayon, A. de la Calle. *Dynamic Modelling of a Continuous Hydrogen Production Plant Based on CeO2 Thermochemical Cycle*. In *API Proceedings of SolarPACES 2017 (under*

revision); 2018.

[55] B. Meredig, C. Wolverton. *Phys. Rev. B - Condens. Matter Mater. Phys.* **2009**, *80*, 1–8, DOI: 10.1103/PhysRevB.80.245119.

[56] J. E. Miller, A. H. McDaniel, M. D. Allendorf. *Adv. Energy Mater.* **2014**, *4* (2), DOI: 10.1002/aenm.201300469.

[57] S. Li, V. M. Wheeler, A. Kumar, M. B. Venkataraman, C. L. Muhich, Y. Hao, W. Lipiński. *Energy Technol.* **2021**, *2000925* (19), 1–18, DOI: 10.1002/ente.202000925.

[58] S. Li, V. M. Wheeler, P. B. Kreider, W. Lipiński. *Energy and Fuels* **2018**, *32* (10), 10838–10847, DOI: 10.1021/acs.energyfuels.8b02081.

[59] M. Hoes, C. L. Muhich, R. Jacot, G. R. Patzke, A. Steinfeld. *J. Mater. Chem. A* **2017**, *5*, 19476–19484, DOI: 10.1039/C7TA05824A.

[60] P. Furler, J. R. Scheffe, M. Gorbar, L. Moes, U. Vogt, A. Steinfeld. *Energy & Fuels* **2012**, *26* (11), 7051–7059, DOI: 10.1021/ef3013757.

[61] D. Marxer, P. Furler, M. Takacs, A. Steinfeld. *Energy Environ. Sci.* **2017**, *10* (5), 1142–1149, DOI: 10.1039/c6ee03776c.